

Eruption dynamics of Hawaiian-style fountains: the case study of episode 1 of the Kīlauea Iki 1959 eruption

Wendy K. Stovall · B. F. Houghton · H. Gonnermann ·
S. A. Fagents · D. A. Swanson

Received: 25 March 2010 / Accepted: 18 October 2010 / Published online: 26 November 2010
© Springer-Verlag 2010

Abstract Hawaiian eruptions are characterized by fountains of gas and ejecta, sustained for hours to days that reach tens to hundreds of meters in height. Quantitative analysis of the pyroclastic products from the 1959 eruption of Kīlauea Iki, Kīlauea volcano, Hawai‘i, provides insights into the processes occurring during typical Hawaiian fountaining activity. This short-lived but powerful eruption contained 17 fountaining episodes and produced a cone and tephra blanket as well as a lava lake that interacted with the vent and fountain during all but the first episode of the eruption, the focus of this paper. Microtextural analysis of Hawaiian fountaining products from this opening episode is used to infer vesiculation processes within the fountain and shallow conduit. Vesicle number densities for all clasts are high (10^6 – 10^7 cm⁻³). Post-fragmentation expansion of

bubbles within the thermally-insulated fountain overprints the pre-fragmentation bubble populations, leading to a reduction in vesicle number density and increase in mean vesicle size. However, early quenched rims of some clasts, with vesicle number densities approaching 10^7 cm⁻³, are probably a valid approximation to magma conditions near fragmentation. The extent of clast evolution from low vesicle-to-melt ratio and corresponding high vesicle number density to higher vesicle-to-melt ratio and lower vesicle-number density corresponds to the length of residence time within the fountain.

Keywords Hawaiian fountaining · Kīlauea · Kīlauea Iki · Vesicle size distribution · Post-fragmentation expansion

Editorial responsibility: D.B. Dingwell

W. K. Stovall (✉) · B. F. Houghton
Department of Geology and Geophysics,
University of Hawai‘i at Mānoa,
1680 East-West Road,
Honolulu, HI 98622, USA
e-mail: wstovall@soest.hawaii.edu

H. Gonnermann
Department of Earth Science, Rice University,
6100 Main Street,
Houston, TX 77005, USA

S. A. Fagents
Hawai‘i Institute of Geophysics and Planetology,
University of Hawai‘i at Mānoa,
1680 East-West Road,
Honolulu, HI 98622, USA

D. A. Swanson
U.S. Geological Survey, Hawaiian Volcano Observatory,
P.O. Box 51, Hawai‘i National Park, HI 96718, USA

Introduction

Hawaiian-style eruptions and Kīlauea Iki

Hawaiian fountains (Fig. 1) produce jets of gas and basaltic tephra, and Kīlauea volcano (Fig. 2) is the type locality for this eruptive style (e.g., Heliker and Mattox 2003; Richter et al. 1970; Swanson et al. 1979). Hawaiian fountains have also been observed at many other basaltic volcanoes (e.g., Bertagnini et al. 1990; Fedotov et al. 1980). Here we assess processes in the shallow conduit and fountain during the first episode of the 1959 Kīlauea Iki eruption.

The eruption began from a line of fissures on the wall of an existing pit crater on November 14, 1959 (Fig. 2). Prior to 1959, the eastern base of the pit was 85 m below that of the western part of the pit (Richter et al. 1970). The main vent for the Kīlauea Iki eruption was located 20 m above the floor of the western side of the pit. Seventeen episodes lasted 36 days, producing a tephra blanket extending ~15 km

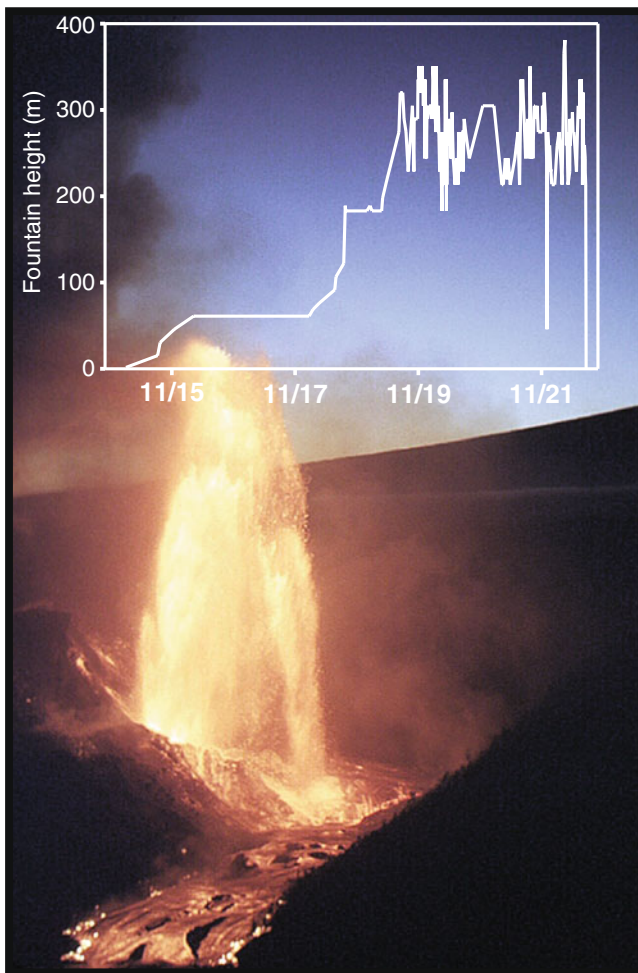


Fig. 1 Photograph of Kīlauea Iki episode 1 fountain with inset plot of fountain height with time. Taken November 18, 1959 by J. Eaton. Fountain height data collated from Richter et al. 1970 and unpublished archives (D. Richter and J. Eaton notebooks and photographs)

downwind, a ~64-m-high cone, and a $3.7 \times 10^7 \text{ m}^3$ lava lake within the pit crater. With the exception of the weak episode 17, each episode had two phases. The first phase consisted of fountaining activity (Fig. 1) and coincident filling of the adjacent lava lake which eventually overtopped the vent. The second phase commenced when fountaining ceased and lava drained from the lake, back down the vent. The durations of fountaining phases of each episode varied, lasting from 9 h to 7 days (for episode 1) with peak fountain heights between ~30 m and ~580 m.

Purpose

This paper supplies a quantitative analysis of Hawaiian fountaining using the initial episode of the Kīlauea Iki eruption as a case study. We combine (1) observational data from Kīlauea, (2) microtextural analyses of pyroclasts, (3) computational models of vesiculation and (4) conceptual

models for Hawaiian eruptions. We develop increased insight into post-fragmentation processes within the fountain and expand on Cashman and Mangan (1994) by comparing carefully selected single clasts collected over narrow stratigraphic intervals.

Background and previous work

Previous vesicularity studies of Hawaiian ejecta

Cashman and Mangan (1994) and Mangan and Cashman (1996) conducted the first microtextural analysis of Hawaiian ejecta using pyroclasts from 1984 to 1986 Pu‘u Ō‘ō fountaining. Vesicle diameter measurements were made using photomicrographs but were constrained by the 0.01 cm resolution of the digitizing tablet used for measurement.

Two clast types were defined based on texture and vesicularity (Mangan and Cashman 1996). ‘Scoria’ consists of closed-cell foam of $\leq 85\%$ vesicularity, with round, undeformed, broadly-sized vesicles. Vesicle data for scoria shows some coalescence, number densities between 1.8×10^5 and $1.9 \times 10^4 \text{ cm}^{-3}$, nucleation rates near $2 \times 10^4 \text{ events cm}^{-3} \text{ s}^{-1}$, and a growth rate of $9 \times 10^4 \text{ cm s}^{-1}$. ‘Reticulite’ has $>95\%$ vesicularity and is an open-cell polyhedral foam with $\sim 1 \text{ }\mu\text{m}$ thick vesicle walls. Reticulites have number densities between 1.8×10^3 and $1.1 \times 10^2 \text{ cm}^{-3}$, and it was inferred that the scoria to reticulite transition is a consequence of Ostwald ripening, whereby larger bubbles grow at the expense of smaller bubbles. Mangan and Cashman (1996) infer that the textural contrast between the scoria and reticulite relates to post-fragmentation expansion of clasts within the fountain. Scoria preserves textures closer to conditions upon fragmentation, whereas continued vesiculation and clast expansion in the thermally-insulated core of the fountain results in reticulite.

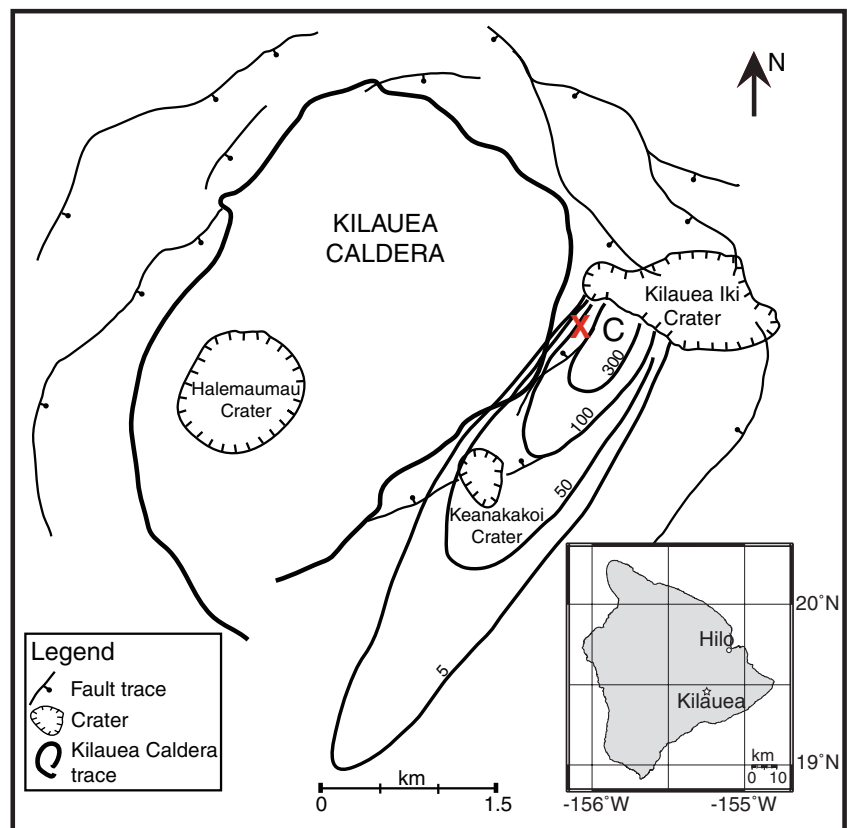
Contemporary unpublished data for Kīlauea Iki 1959

USGS Hawaiian Volcano Observatory and Hawai‘i Volcanoes National Park (HVNP) house archives of observations from the eruption. Field notebooks from both sources record tephra thicknesses, fine-scale height fluctuations, and behaviors of the lava fountain. Photograph archives, from Jerry Eason and Don Richter, are stamped with time and date and include descriptive comments relating to photograph location and fountain height.

Review and significance of episode 1

Richter et al. (1970) give a chronology of the 1959 eruption which is summarized below. The eruption began at 16:08

Fig. 2 Location map of Kīlauea caldera and episode 1 study site. **a** Kīlauea Caldera and Kīlauea Iki crater with tephra isopachs (thickness in cm, Houghton, unpublished data, 2008), Pu‘u Pua‘i cone summit (C), and tephra pit study site (X). **b** Island of Hawai‘i with star marking location of Kīlauea



on November 14 when ten fissure segments opened along ~900 m of the south wall of the pit crater. Initial fountains to 30 m in height fed a lava pond at the base of the east pit. By the afternoon of November 15, the outermost vents had died and the eruption was centered at a single western location. The flux increased, and the single fountain reached greater heights, raining ejecta downwind to form the Pu‘u Pua‘i (gushing hill) tephra cone (Fig. 2). Fountains during the last 5 days of the first episode fluctuated between 200 and 300 m high (Fig. 1). On November 20, Richter et al. (1970) noted that “... occasionally hot gas, without liquid lava, burst out with almost explosive violence between the cone and fountain.” This indicates that there were periods when outgassing was unaccompanied by a flux of magma (Richter et al. 1970). The gas component formed a dilute convective thermal plume above the fountain, carrying small quantities of finer particles and pumice downwind. On the morning of November 21, the lava lake reached the vent level, but fountaining continued through the lake surface. Spatter ramparts extending from the cone into the lake acted to stabilize the vent. However, at 19:25, within 40 s, the fountain fell from ~210 m to zero height. Drainback of the lava lake was first noticed on November 22 and continued through November 23.

This first and longest fountaining phase of the Kīlauea Iki eruption lasted for 7 days, reached a peak fountain height of 380 m (Fig. 1), and produced the greatest volume of ejecta (nearly $31 \times 10^6 \text{ m}^3$ in the lava lake). Subsequent fountaining phases lasted 2–32 h and had variable fountain peaks between 30 and 580 m (Fig. 1), the latter the highest lava fountain recorded in Hawai‘i. Because of lava drain-back after each fountaining phase, early fountains from episodes 2–17 had to clear the conduit of residual, relatively-outgassed lava. In contrast, episode 1 had no influence of drained-back lake lava.

This eruptive episode resembled other classical high Hawaiian fountaining eruptions such as Mauna Ulu in 1969 (Swanson et al. 1979) and Pu‘u ‘Ō‘ō between 1983 and 1986 (Heliker and Mattox 2003). These eruptions also started as fissures which evolved into a single vent that progressed from low to high fountaining. Typically, activity ended rapidly with surges in eruption rate/height before fountaining abruptly ceased (Swanson et al. 1979).

Deposit characteristics

We studied the stratigraphy of the 1959 eruption in 200 tephra pits extending from 300 m to 5 km down wind of Pu‘u Pua‘i. These data were compared to data collected

during the eruption by HVO scientists, who probed the depth of the tephra along a cross-wind traverse after episodes 1, 3, 11 and the close of the eruption.

Figure 3 includes the stratigraphy, grain size data and samples with selected density distributions for tephra from the episode 1 study site, KI-07-07 (Fig. 2). Because this location is ~50 m above vent level, the fountain had to reach at least this height before deposition commenced in this area.

Contemporary photographs (J. Eaton) correlate the onset of tephra fall on the crater rim with the late morning of November 17, when the fountain reached ~75 m (Fig. 1).

Episode 1 clasts are black to golden, commonly with a shiny, glassy rind (Fig. 4). Achnelith lapilli (Walker and Croasdale 1972) dominate the clast population. Pele's tears and hair occur in the lower portion of the deposit (Fig. 3) with scattered pumice near the base.

Fig. 3 Kīlauea Iki episode 1 stratigraphy, grain size, and bulk density. **a** Stratigraphy with sample locations and **b** median grain size and maximum clast diameter. **c** Density distributions for samples taken from locations labeled in stratigraphy, vertical line drawn through 1,100 kg/m³ to assist comparison, dots above histograms indicate mean density, bars equal 1 standard deviation. Maximum clast diameters are calculated from the average of three axes for each of 5 clasts. Clasts from samples labeled with larger font are used in this study for microtextural analysis

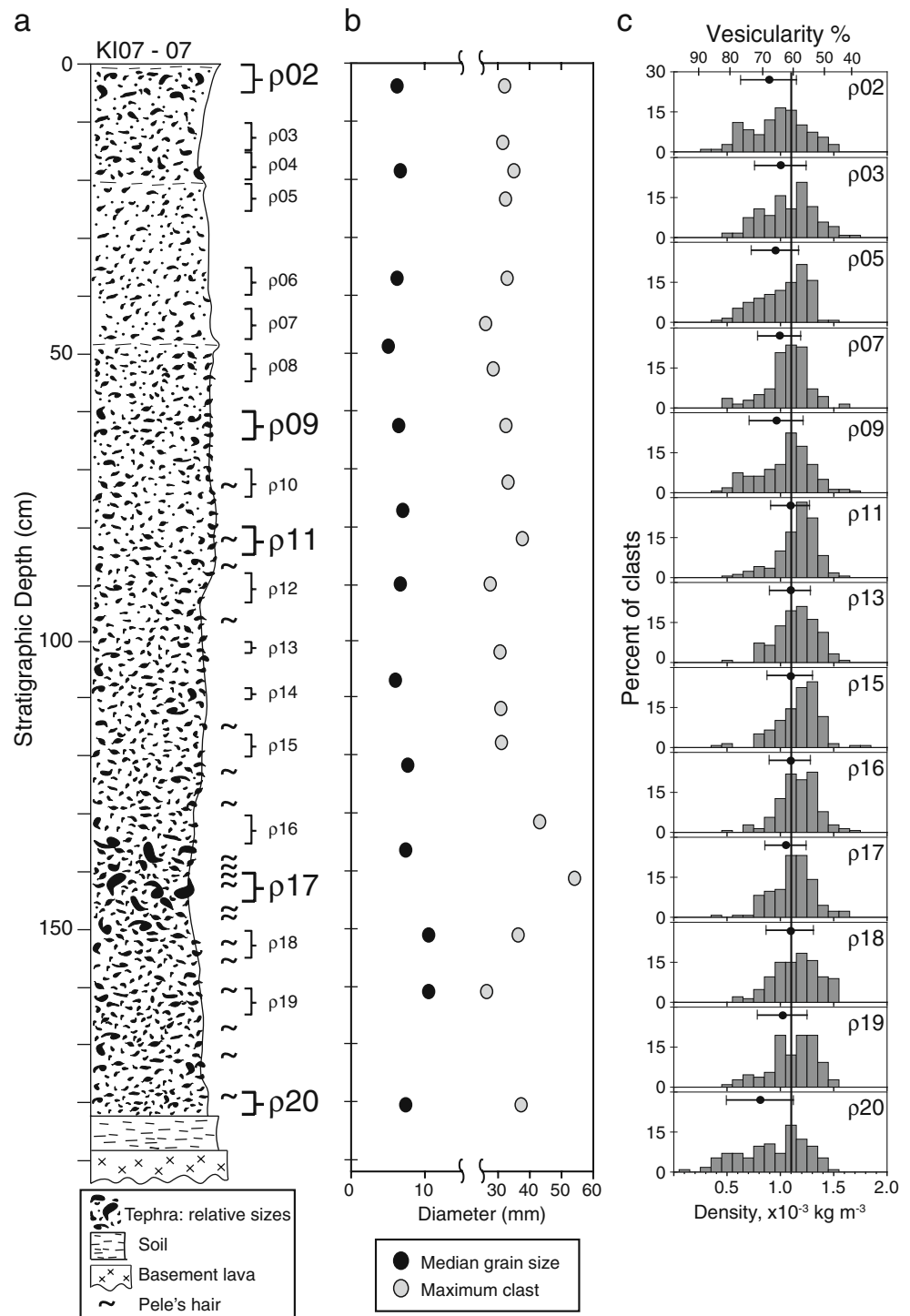
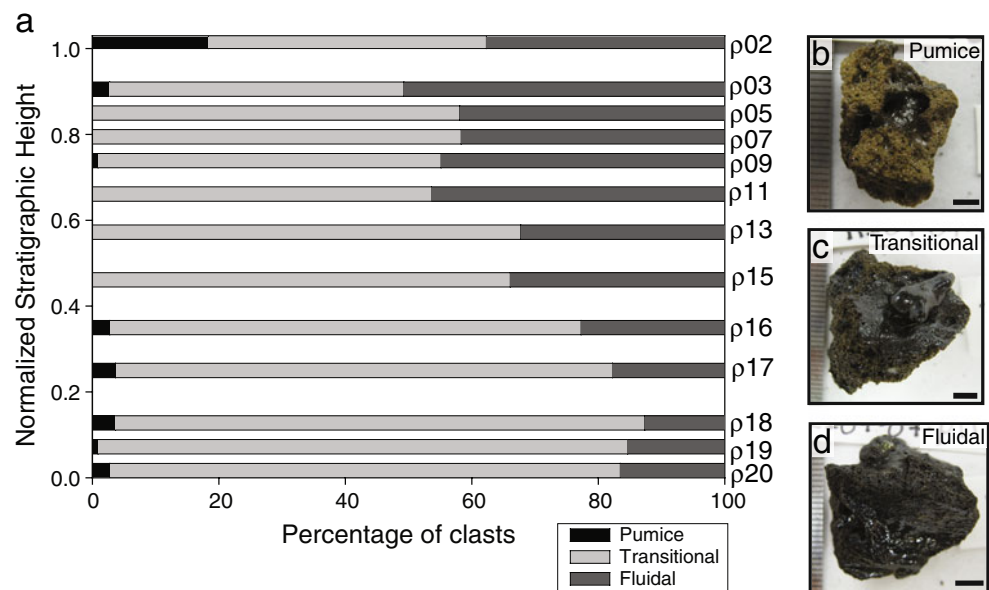


Fig. 4 Componentry and clast photographs for episode 1 samples. **a** Componentry for Kīlauea Iki episode 1 with associated samples labeled and clast-types with 5 mmbar for scale: **b** pumice, **c** transitional, and **d** fluidal. Componentry data are derived from processing samples of at least 100 clasts of diameter 16–32 mm



The median grain size (Fig. 3b) of samples has a narrow range, between -2.4 and -3.4ϕ (5–11 mm) with the coarsest clasts in the lower portion of the sequence. The five largest clasts were measured from each sample, then averaged to yield the mean maximum clast size (Fig. 3b). The largest clasts are located 135 to 150 cm from the top of the section.

Techniques

Sampling

Samples of juvenile lapilli were taken from the tephra pit at our study site (Fig. 2) and used to quantify changes in bulk density and vesicularity of the clast population. Nineteen 5-cm thick samples were collected at approximately 10-cm-spaced intervals (Fig. 3a). Sample locations were chosen to record significant relative changes in clast size and abundance of clast types, sometimes resulting in more closely spaced samples. Each sample consisted of between 120 and 150 clasts, 16–32 mm diameter.

Description of clast morphologies

Juvenile clasts were classified into two textural end members and one intermediate category (Fig. 4). ‘Fluidal’ clasts (Fig. 4d) have dark and shiny surfaces that show external flow lines and are dark brown to black with thick glass walls between mm- to cm-sized bubbles (Fig. 5d, g). ‘Pumices’ (Fig. 4b) are ragged, fragile, and golden to light brown, with thin bubble walls and abundant mm- to sub-mm sized bubbles. Some pumices have shiny outer surfaces but are less dense and paler than the fluidal clasts (Fig. 4d). A third category, ‘transitional’, (Fig. 4c) spans the textural

range between fluidal and pumice. In hand specimen, this group contains domains of either 1) ragged, brown to golden, microvesicular material in an otherwise dark-colored clast containing thick glass between measurable vesicles or 2) darker brown glass that is not dominantly microvesicular within golden, microvesicular material. Transitional clasts commonly have glassy outer surfaces.

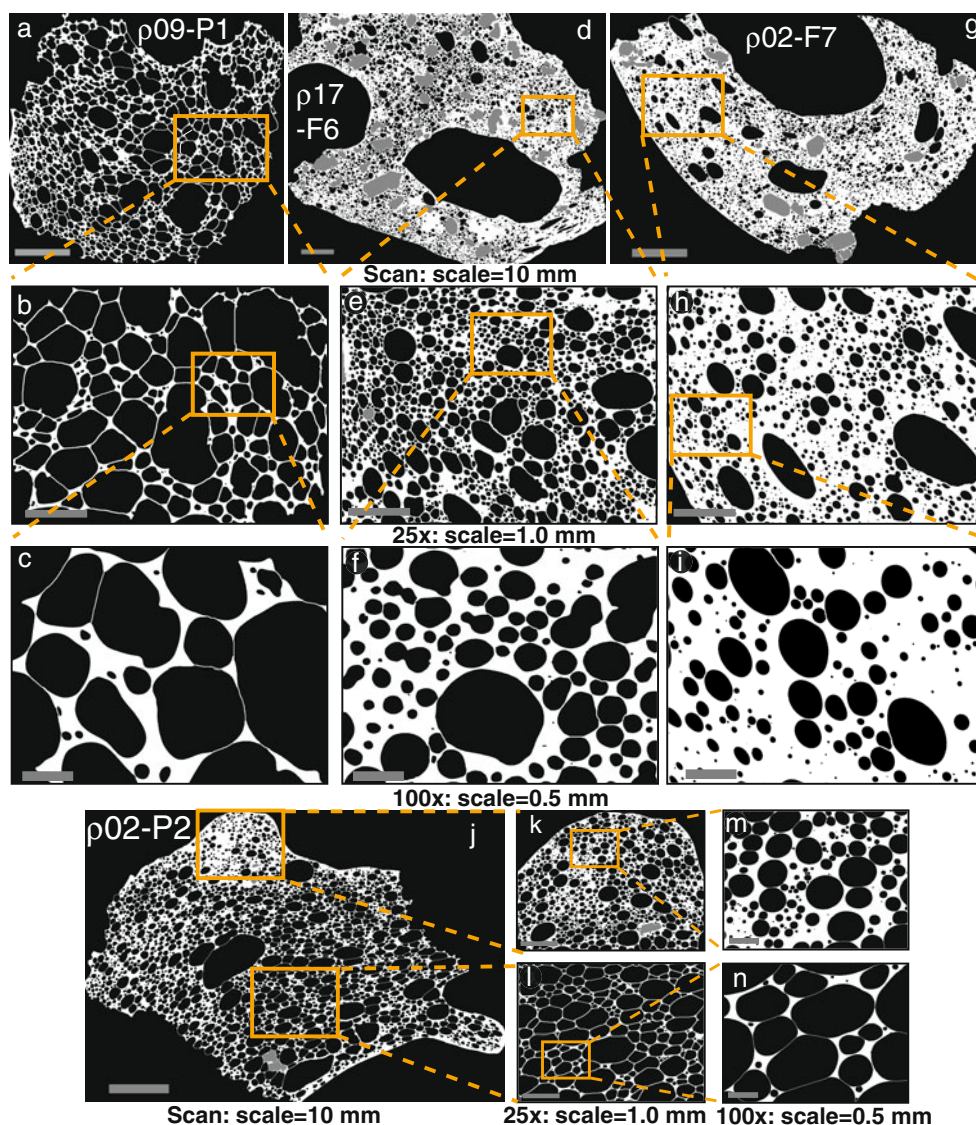
Density and bulk vesicularity

A selection of 13 samples (Fig. 3c) was chosen, for further study, based on stratigraphic position and to bracket abrupt shifts in grain size. All samples from the basal 60 cm, where the most variability in grain size occurs, were included. Above that level every second sample was chosen together with the very top sample. The 13 density samples contain a total of 1,822 pyroclasts from the episode 1 deposit. Density measurements were made on clasts after Houghton and Wilson (1989) using a dense rock equivalent (DRE) value of $2,800 \text{ kg/m}^3$. These vesicularity values are not truly representative of the matrix vesicularity because thin sections reveal relatively high but variable phenocryst contents. Correction for phenocryst percentages results in higher vesicularities (Table 1).

Textural analysis

Samples for thin sections were chosen using the density data (Fig. 3c). We included the top and bottom sample ($\rho 02$ and $\rho 20$) to capture the escalation and termination of high fountaining. Textural analysis was conducted on two clasts from the modal density peak(s), as well as one high- and one low-density clast from each sample, for a total of 19 thin sections. Nested image sets were made using three magnifications (Scan, $25 \times$ and $100 \times$; e.g., Figs. 5 and 6). The

Fig. 5 Grayscale image nests for episode 1 pumice and fluidal clasts. (a through i) Selected clasts displaying typical pumice and fluidal vesicle textures. Thin section scans in the top row, SEM 25 \times magnification in second row, SEM 100 \times magnification in third row. (j through n) Contrasting nests of images for rind and interior of a pumice clast. Vesicles are *black*, glass is *white* and crystals are *gray*



scanned images were captured at 1,200 dpi using transmitted light on an HP flatbed scanner, and higher magnifications were collected using a JEOL-5900LV SEM operating at 15 kV accelerating voltage and 1 nA beam current in backscatter mode (BSEI). Image processing and quantitative vesicle analyses were conducted using the methods outlined in Shea et al. 2009. Of the 19 clasts analyzed, 12 (clasts listed in Fig. 7) have homogeneous textures. Regions within three heterogeneous clasts (listed in Fig. 8) were analyzed separately for comparison with each other and with homogeneous clasts.

Results

Density and bulk vesicularity

The most diverse samples are at the top and bottom of the deposit (Fig. 3c). Clast populations from $\rho 20$ show the widest

density range (50–1,400 kg/m³) and include the greatest percentage of high vesicularity (low density) clasts. $\rho 02$ has a similarly broad yet bimodal density distribution (290–1,450 kg/m³). All other samples have primarily unimodal density distributions and means between 950 and 1,090 kg/m³. The most vesicular clasts are pumice; the fluidal clasts are typically the least vesicular. Transitional clasts span a range of vesicularity from ~50–90% with a mean near 60%.

Qualitative microtextural observations

The episode 1 clasts are dominated by round vesicles, ranging in diameter from 5 μ m to a few centimeters (e.g., Figs. 5, 6 and 9). Textures vary from clasts with relatively homogeneous populations of many vesicle sizes (Fig. 5a, d, g) to others with preferential clusters of smaller and larger vesicles (Figs. 5j and 6f). A significant number of clasts possess texturally distinct rims (Figs. 5j, k and 6f–i), characterized by

Table 1 Episode 1 quantitative vesicle data

Sample (KI07-07)	Density $\times 1,000$ (kg m ⁻³)	Vesicularity ^a (%)	Phenocryst Corrected Vesicularity ^b (%)	N _{A_{tot}} ^c (cm ⁻²)	N _{V_{tot}} ^d (cm ⁻³)	N ^m _{V_{tot}} ^e (cm ⁻³)
ρ09-P1	0.34	87.9	87.9	2.6E+03	6.6E+05	5.4E+06
ρ17-P1	0.40	85.7	85.7	2.9E+03	7.8E+05	5.4E+06
ρ09-T6	0.52	81.4	84.5	4.2E+03	5.6E+05	4.1E+06
ρ11-T13	0.54	80.7	80.7	8.3E+03	1.7E+06	8.9E+06
ρ02-T40	0.59	78.9	78.9	9.1E+03	2.4E+06	1.1E+07
ρ02-T37	0.91	67.5	68.0	7.6E+03	2.1E+06	6.6E+06
ρ09-T29	1.09	61.1	65.1	1.0E+04	4.2E+06	1.2E+07
ρ09-T82	1.31	53.2	58.2	8.3E+03	4.6E+06	1.1E+07
ρ17-F6	1.12	60.0	67.5	5.7E+03	9.4E+05	3.8E+06
ρ20-F9	1.40	50.0	64.2	1.1E+04	2.4E+06	6.6E+06
ρ11-F12	1.50	46.4	57.6	1.2E+04	6.8E+06	1.6E+07
ρ02-F7	1.40	50.0	53.8	8.6E+03	3.9E+06	8.4E+06
ρ02-P2 rind		55.1 ^f		9.4E+03	4.4E+06	9.9E+06
ρ02-P2 interior		79.6 ^f		1.1E+03	1.9E+05	9.2E+05
ρ20-P5 rind		59.5 ^f		8.8E+03	4.3E+06	1.1E+07
ρ20-P5 interior		73.3 ^f		1.2E+03	5.8E+05	2.2E+06
ρ11-T19 rind		42.8 ^f		1.2E+04	5.8E+06	1.0E+07
ρ11-T19 interior		74.9 ^f		3.5E+03	8.4E+05	3.3E+06

^a Vesicularity calculated from density and DRE of 2,800 kg m⁻³ computed using formula of (Bottinga and Weill 1970) based on chemical composition of the glass from tephra sample S-5 collected on November 18, 1959 at 5:00 p.m. (Murata and Richter 1966)

^b Vesicularity calculated from density of clast minus percent density of olivine. Percent of olivine was determined by area of clast containing olivine in thin section

^c N_{A_{tot}} is the number of vesicles per unit area of clast matrix with phenocrysts subtracted. Values are the sum of bins from 0.005 to 40 mm

^d N_{V_{tot}} is the number of vesicles per unit volume of clast matrix with phenocrysts subtracted

^e N^m_{V_{tot}} is referenced to melt only, calculation based on phenocryst corrected (e) or N_{V_{tot}}-derived (f) vesicularity

^f N_{V_{tot}}-derived vesicularity

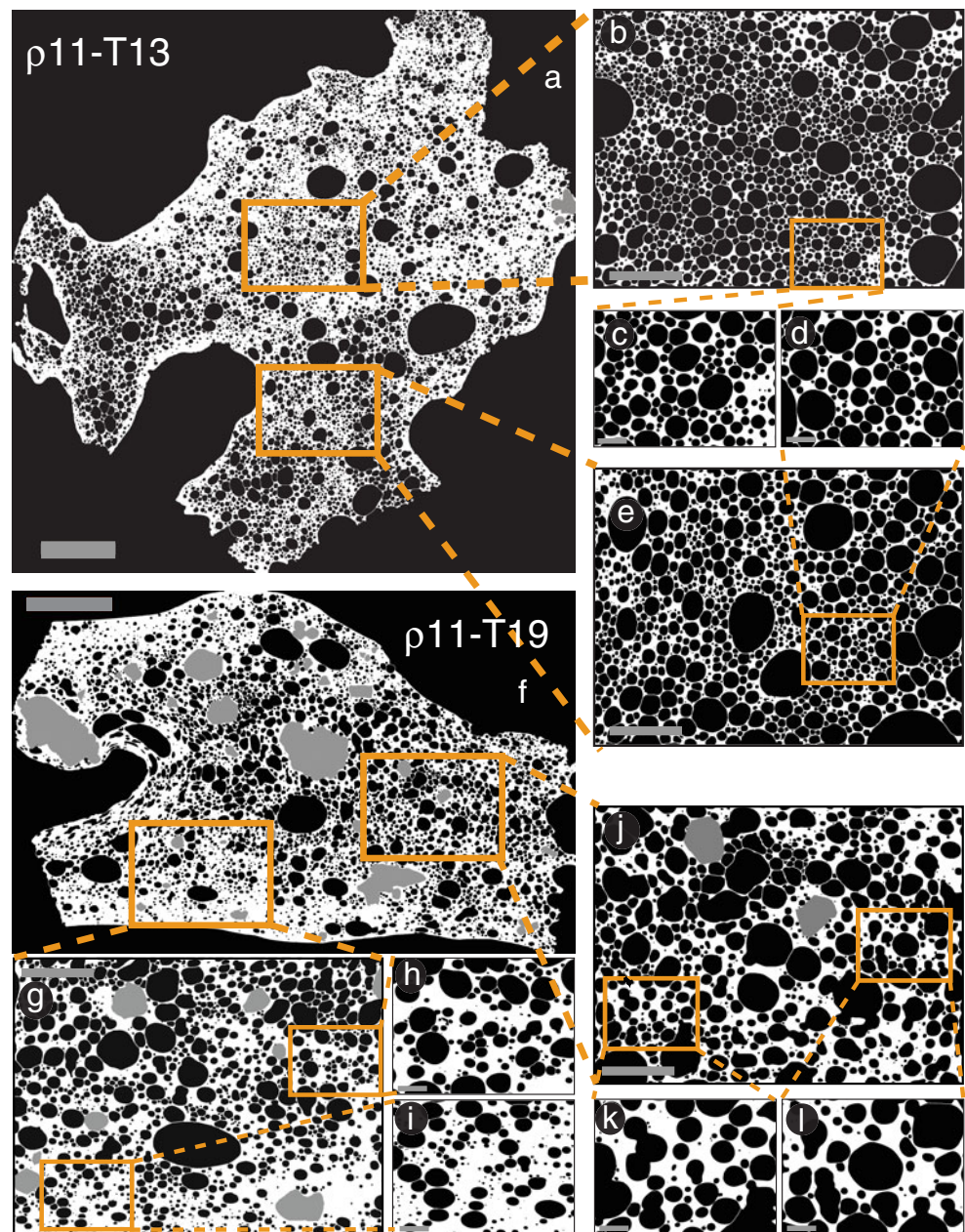
small vesicles (<0.01–0.1 mm in diameter), enclosing zones containing larger vesicles (1–>4 mm in diameter) (e.g., Figs. 5j, l and 6f, j–l). Local elongation of vesicles occurs in some clasts and mimics the shape of the clast exterior (Figs. 5d, g and 6f). Coalescence textures are visible as outsized, typically amoeboid, vesicles (Figs. 5a, 6f and 9a), some with irregular bubble walls (Fig. 5b). Pumice clasts lack small vesicles and contain dominantly intermediate-sized vesicles with very thin (one-μm-wide) bubble walls (Fig. 5a, l). In the extreme case, these bubbles take on polygonal shapes. Fluidal clasts contain a more uniform population of many vesicle sizes (Fig. 5d, g). In general, in contrast to pumice, fluidal clasts are marked by smaller vesicle sizes and greater wall thicknesses (Fig. 5).

Transitional clasts span, in the broadest sense, a range of textures intermediate between fluidal clasts and pumice. Figure 6 illustrates two extremes. In one case (Figs. 6a and 9a, d), the clasts contain a very narrow rim on unbroken surfaces characterized by small vesicles enclosing a broad

homogeneous core with markedly larger vesicles and thinner bubble walls. In ρ11-T13, the homogeneous bubble size distribution in the interior of the clast is clearly visible in the similarities between the two 25 × images in Fig. 6 (b, e) and between the two nested 100 × images (Fig. 6c, d). In such ‘homogeneous’ transitional clasts (Fig. 9), the range of vesicle textures spans amoeboid vesicles with thinner glass walls (Fig. 9a–c) to round vesicles with thicker walls (Fig. 9d–f).

In the other extreme, two different textures are seen, defining regions with gradational boundaries (Fig. 6f); we call these ‘heterogeneous’ transitional clasts. One type of region, commonly extending inward from the margins of the clasts, consists of relatively small uniform vesicles, in microlite-free glass (Fig. 6f). The other, generally in the interior of the clast, contains populations of much more widely spaced and typically slightly larger vesicles (Fig. 6f). These contrasts extend to all bubble sizes, as seen by comparing the two nests of 25 × and 100 × images (Fig. 6g–l).

Fig. 6 Grayscale image nests for homogeneous and heterogeneous transitional clasts. Image nests of a homogeneous-transitional (a–e) and a heterogeneous-transitional (f–l) clast. Scale on binary thin section scans (a, f) is 10 mm, scale on SEM 25 \times magnification (b, e, g, j) is 1.0 mm, and scale on SEM 100 \times magnification (c, d, h, i, k, l) is 0.5 mm



Olivine phenocrysts and oxide microphenocrysts are common in all except the most vesicular clasts, simply because there is less melt available to house the crystals in the more vesicular clasts. Phenocryst distribution shows no correlation with vesicle distribution (Figs. 5b–c and 6). Microlites are rare and, when present, do not influence bubble shape.

Quantitative microscopic vesicle data

Vesicle size data are used to determine roles of bubble nucleation, growth and coalescence from the time of fragmentation until quenching of the clasts. Vesicle volume distributions (VVDs) (Fig. 7) represent the volume fraction of vesicles in a given geometric size range (bin) for the 12

analyzed homogeneous clasts. In 9 of 10 clasts with <81% vesicularity (Fig. 7), there are significant numbers of 5–10 μm vesicles that account for a low volume percentage and thus do not appear on the VVD plots. Therefore, the x-axis has been truncated to show only those bins where the data are clearly visible on the histograms.

In Fig. 7 homogeneous clast VVDs are organized by textural type and vesicularity. VVDs show multiple peaks, and the strongest correlation across the majority of clasts is a peak at 0.25 mm diameter, seen in 8 of 12 clasts analyzed. The coarsest vesicle modes are consistently in high-vesicularity pumice clasts (right column, Fig. 7), which are bimodal with peaks at 0.40–0.63 mm and 2.50–4.00 mm diameter. Fluidal clasts contain a single mode at

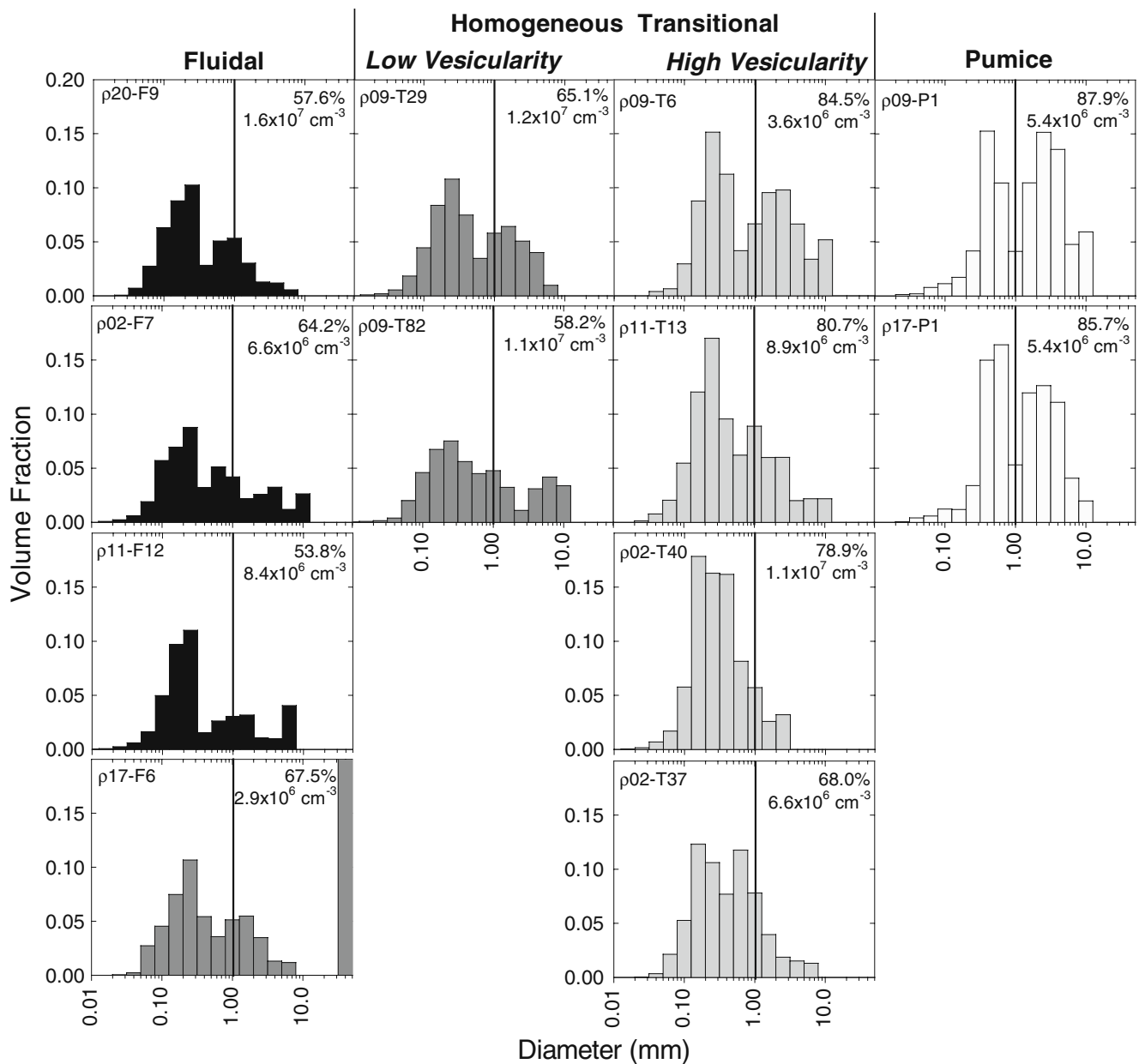


Fig. 7 Vesicle volume distributions for homogeneous episode 1 clasts. Distributions of volume fraction of vesicles within a specific size range (VVD) arranged according to vesicularity and vesicle number density. Sample number, vesicularity, and vesicle number

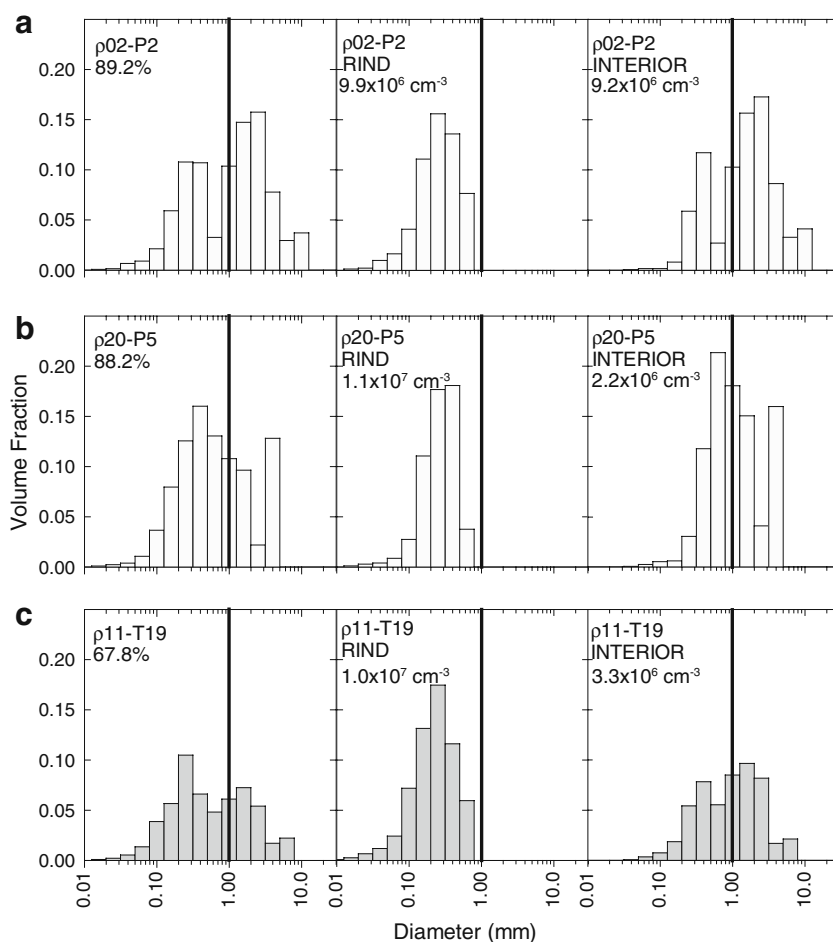
density per cubic centimeter included with each histogram (also found in Table 1). *Dark- to light-gray shading* corresponds with vesicularity grouping. *Vertical lines* are drawn at 1.0 mm vesicle diameter to assist comparison

0.25 mm diameter with few vesicles >1.00 mm diameter. VVDs for homogeneous transitional clasts span the range between those of pumice and fluidal clasts. There is a weak trend in the homogeneous-transitional clasts with vesicularity. In the ‘high vesicularity’ column, vesicle volumes for bubbles <1.00 mm diameter increase as vesicularity increases until the vesicle population coarsens at the expense of smaller diameter classes.

Vesicle number densities (VNDs) (Table 1), were measured as vesicles per unit area ($N_{A_{tot}}$, cm^{-2}) and converted to vesicles per unit volume ($N_{V_{tot}}$, cm^{-3}). Melt-

corrected VNDs ($N_{V_{tot}}^m$, Table 1) are the number of vesicles per unit volume of melt, (following Klug et al. 2002) rather than bulk rock ($N_{V_{tot}}$). $N_{V_{tot}}$ values range from $5.6 \times 10^5 \text{ cm}^{-3}$ to $6.8 \times 10^6 \text{ cm}^{-3}$ (Table 1, $N_{V_{tot}}^m = 3.8 \times 10^6 \text{ cm}^{-3}$ to $1.6 \times 10^7 \text{ cm}^{-3}$). In comparison to other dry basaltic eruptions, our bulk number densities are higher than those for both lava flows from Kīlauea ($\sim 10^3 \text{ cm}^{-3}$; Mangan et al. 1993), and from previous studies of Hawaiian reticulite and scoria ($1.1 \times 10^2 \text{ cm}^{-3}$ to $1.8 \times 10^5 \text{ cm}^{-3}$; Mangan and Cashman 1996) and moderately higher than lapilli from Stromboli volcano ($N_{V_{tot}} = 9.3 \times$

Fig. 8 Vesicle volume distributions for rinds and interiors of heterogeneous clasts. Volume fraction of vesicles within specific size ranges for heterogeneous clasts exhibiting textural differences between the rind and interior of clasts. VVD distributions in this case are used for qualitative comparison only. Whole clast vesicularity and VVD included in left column. Separate rind and interior vesicle volume distributions include quantitatively comparable number of vesicles per square centimeter (also found in Table 1)



10^4 to $1.3 \times 10^6 \text{ cm}^{-3}$; $N_{V_{\text{tot}}} = 1.9 \times 10^5$ to $3.4 \times 10^6 \text{ cm}^{-3}$; Lautze and Houghton 2007). However, our VNDs partially overlap those for products from Villarrica volcano on the low end ($N_{V_{\text{tot}}} = 6.4 \times 10^4$ to $2.1 \times 10^6 \text{ cm}^{-3}$; $N_{V_{\text{tot}}} = 7.4 \times 10^5$ to $1.4 \times 10^7 \text{ cm}^{-3}$; Gurioli et al. 2008), and from the 122 BC Etna basaltic Plinian eruption on the high end ($N_{V_{\text{tot}}} = 2.6 \times 10^6$ to $6.1 \times 10^7 \text{ cm}^{-3}$; Sable et al. 2006). The span of episode 1 VNDs also falls within the range of some products of the more powerfully explosive Keanakāko'i tephra at Kīlauea (9.5×10^4 to $1.0 \times 10^7 \text{ cm}^{-3}$; Mastin et al. 2004).

Interpretation

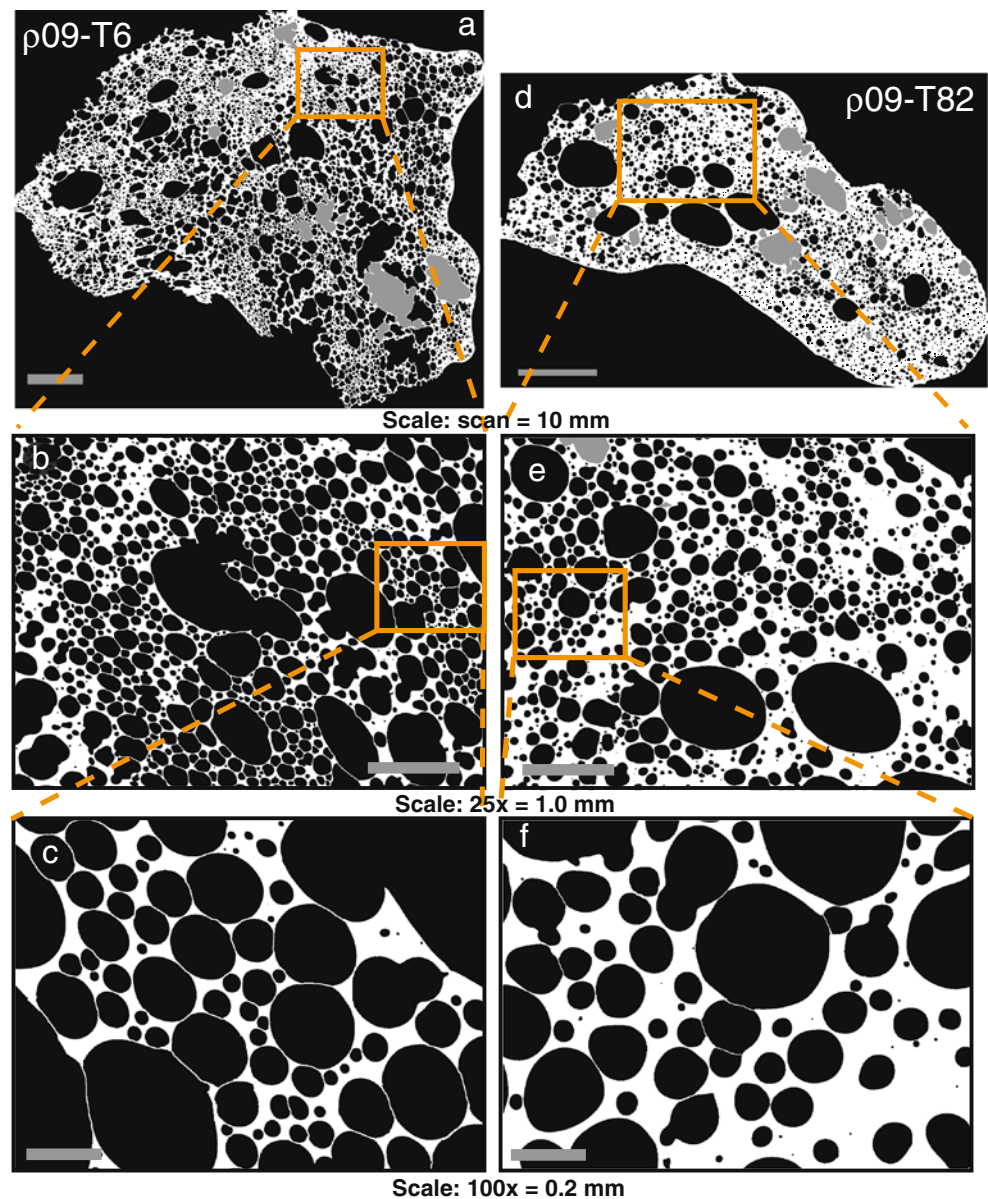
Interpretation of macroscopic data

Morphological differences among clasts (Fig. 4) reflect the abundance and spacing of vesicles. This influences bulk clast density; typically pumices have the lowest, fluidal clasts the highest, and transitional clasts lie between. Vesicles within single clasts, and larger centimeter-scale vesicles imprinted on clast exteriors, indicate that gas

bubbles spanned a large size range, at least 3 orders of magnitude, in the moments prior to fragmentation. Glassy outer surfaces of clasts have been interpreted as a late-stage product of fusion by hot gasses streaming past the ejecta within the fountain (Thordarson et al. 1996).

The slight fluctuations in density and bulk vesicularity in the episode 1 sample suite can be linked to minor changes in eruption and fountain behavior. Probably, the high abundance (Fig. 3c, 18% of ρ_{20}) of easily transportable high-vesicularity (82–98%) clasts at the base of the deposit records relatively light clasts that were partitioned into the dilute convective plume (e.g., Manua Ulu, Swanson et al. 1979) above the low fountain during the first days of the eruption (Richter et al. 1970). The transitional to fluidal clasts within ρ_{20} (Fig. 4) define an overall peak density of $1,100 \text{ kg/m}^3$ (~60% vesicularity) which is slightly lower than overlying samples. Fountain height and mass discharge ramped up during deposition of ρ_{20} , and the majority of clasts landing in the study site during this time probably came from the upper fountain, dominated by lower-density clasts (Parfitt and Wilson 1999). Therefore, the first several centimeters of tephra rich in relatively low-density clasts represents sedimentation from the top of the growing fountain.

Fig. 9 Grayscale image nests for end-member vesicularity of episode 1 homogeneous transitional clasts. Thin-section scans in top row, SEM $25\times$ magnification in middle row, and SEM $100\times$ magnification in bottom row



Samples from most of the deposit have uniform clast densities and corresponding modal vesicularity of 61–66% (Fig. 3c), which is predictable due to the steady sustained nature of the fountain during this period.

Samples from the top of the deposit have similar density distributions to those of the lowermost samples (Fig. 3), but the fountain behaved differently. During the last 10 h, the lake level overtopped the vent and the jet had to penetrate through the overlying lava. This overburden of lava added complexity to the previously steady fountaining. The fountain base widened (D. Richter and J. Eaton photograph archives), and although reaching heights of up to ~ 240 m during the last 10 h, fountaining was not sustained and heights pulsated between that maximum and ~ 100 m until the abrupt end of the episode (Fig. 1). The modes in sample $\rho 02$ (from the top of the sequence) are shifted toward lower densities compared

to most of the deposit, suggesting a proportional increase in the amount of sedimentation from the upper regions of fluctuating fountains. The polymodal $\rho 03$ lies just below $\rho 02$, which contrasts with the strongly unimodal density distributions below this stratigraphic level. Assuming an even sedimentation rate over ~ 4.5 days, ~ 1.7 cm of tephra was deposited every hour. The lava lake reached vent level ~ 8 h before the eruption ceased, which corresponds to the uppermost ~ 13 cm of tephra accumulation, equivalent to $\rho 03$ and $\rho 02$ (Fig. 3a). Therefore, lake-influenced fountain fluctuations are likely responsible for the polymodal density distribution of sample $\rho 03$ clasts (Fig. 3c).

Grain size varies little throughout the deposit (Fig. 3b), and maximum clast sizes have no strong correlation with the median grain size. Based on fountain height (Fig. 1) and the inferred deposition rate, we correlate the level of the largest

clasts (Fig. 3b) with November 18, when the fountain height surged to 320 m for the first time. Median grain size data are typically relied upon to serve as a proxy for eruption intensity (e.g., Sable et al. 2006). The lack of variation exhibited in episode 1 is consistent with the discharge remaining relatively constant with a slight increase on November 18.

Interpretation of quantitative vesicle data

In Hawaiian eruptions, large clasts remain sufficiently hot and fluid to permit considerable post-fragmentation deformation (Mangan and Cashman 1996). Therefore, vesicle data includes both clues to conditions at the moment of fragmentation and to processes occurring after fragmentation. There are features common to all pyroclasts and differences between clasts, both among and within samples, that suggest a role for post-fragmentation processes.

Features common to all pyroclasts

The 1959 clasts have a predominance of simple ellipsoidal to spherical bubble shapes across all size ranges. In this regard they contrast drastically with the vesicle population in basaltic

Plinian pyroclasts (Sable et al. 2006). This suggests that characteristic relaxation times for bubbles (i.e., the time for coalesced bubbles to return to spheres) are generally achieved in the Kilauea Iki fountains, unlike the basaltic Plinian eruptions. In addition, the principal size mode for vesicles in all the pyroclasts is typically 150–350 μm , irrespective of clast vesicularity. We interpret the similarities to reflect the common early history of the melt forming episode 1 pyroclasts. We infer that variability in vesicle size, shape, and distribution reflects later divergence in the patterns of degassing and bubble growth, which we will quantify later, as occurring during post-fragmentation conduit ascent and fountaining. The studied clasts have a wide range in morphology and vesicle size distribution but have very similar $N_{\text{Vtot}}^{\text{m}}$ values. This observation alone suggests that the 1959 melt had a relatively uniform history of bubble nucleation and that textural diversity arose principally in the interval between the cessation of bubble nucleation and quenching.

Textural variability within clasts: rinds and interiors

Each vesiculation process imparts a characteristic signature (Fig. 10) on a plot of vesicle-to-melt ratio (V_G/V_L after

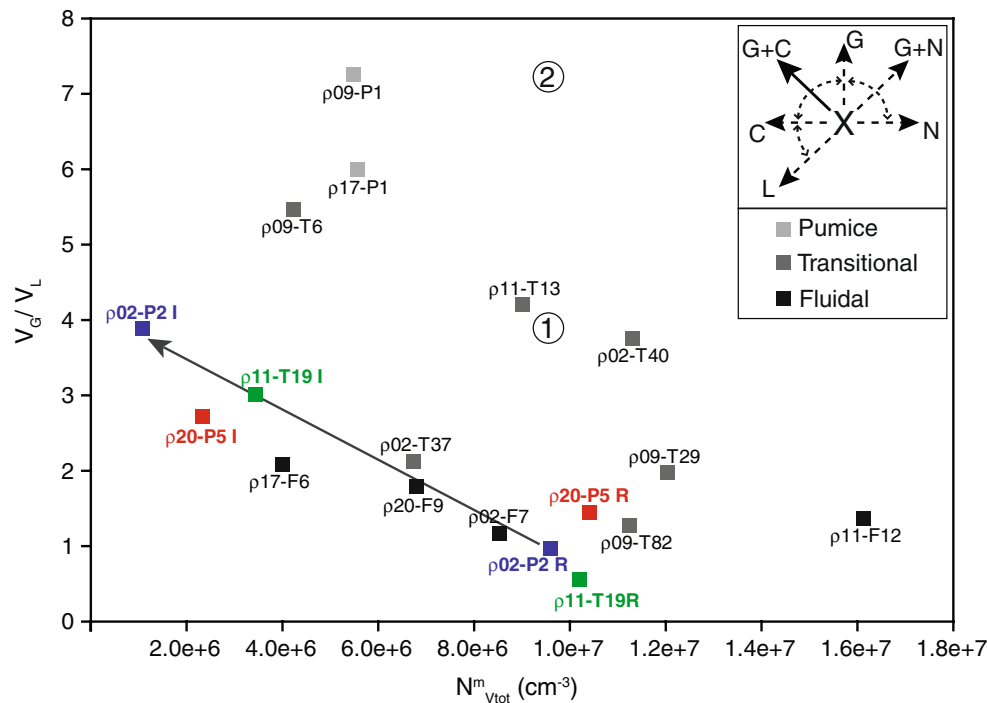


Fig. 10 Volumetric ratio of vesicles to melt (V_G/V_L) versus vesicle number density ($N_{\text{Vtot}}^{\text{m}}$) for episode 1 clasts. Data points are labels of clast name; R (rind) and I (interior) following same clast name indicate data from specific zones. Inset graph depicts vesiculation trends originating at X proceeding via decompressive plus diffusive growth only (G), growth plus nucleation (G + N), nucleation only (N), growth plus coalescence (G + C), coalescence only (C), and bubble loss (L). Our study indicates low V_G/V_L and high $N_{\text{Vtot}}^{\text{m}}$ clasts most

closely resemble melt at the time of fragmentation with further vesiculation processes proceeding from that point. Circled numbers are points used in calculating relative growth and coalescence for melt originating with parameters equal to $\rho_{02}\text{-P2I}$ and expanding to $\rho_{02}\text{-P2I}$ (1) and $\rho_{09}\text{-P1}$ (2) as discussed in the text. The arrow indicates the pathway necessary to achieve the interior texture originating at the rind texture for clast $\rho_{02}\text{-P2}$

Gardner et al. 1996) and VND (Fig. 10). Addition of small bubbles leads to increased VND and only a slight increase in V_G/V_L . Bubble growth by some combination of diffusion and decompression leads to increased V_G/V_L at constant VND. VND decreases while V_G/V_L increases during bubble coalescence, whereas loss of bubbles via collapse or buoyant rise leads to a reduction in both parameters. Intermediate trends on the diagram reflect combinations of more than one of these processes.

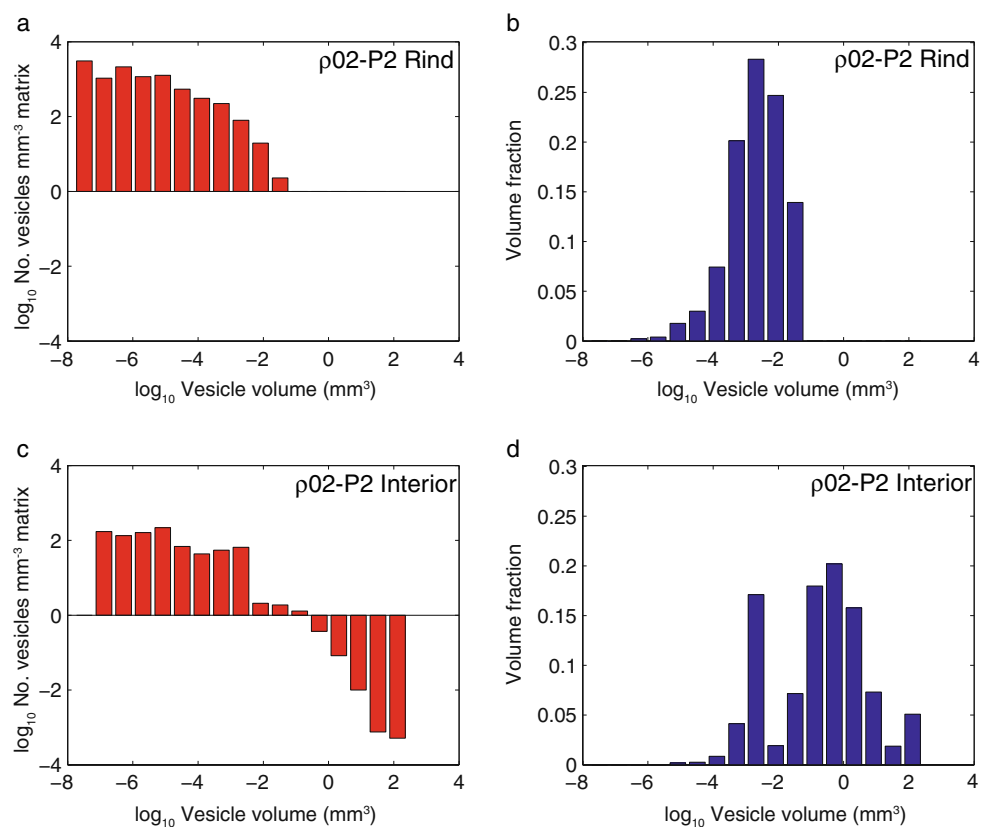
We use an analysis of the pumice clast $\rho 02\text{-P}2$ as a case study to explore the nature of the rims present on pyroclasts. In this clast, a rind characterized by a large number of small vesicles with mm-thick walls (Fig. 5j, k, m) passes inward to a population of larger vesicles with micron-thick walls in the center of the clast (Fig. 5j, l, n). $N_{V_{\text{tot}}}$ values for the rind and clast interior are $4.4 \times 10^6 \text{ cm}^{-3}$ and $1.8 \times 10^5 \text{ cm}^{-3}$ respectively (Table 1). Melt correction of VND was calculated for each zone based on the $N_{V_{\text{tot}}}$ -derived vesicularity, because density-derived vesicularity for individual zones could not be calculated. Based on comparisons of density-derived vesicularity and $N_{V_{\text{tot}}}$ -derived vesicularity for whole clasts, this approximation may result in a $\sim 5\%$ error in the vesicularity calculation. $N_{V_{\text{tot}}}^m$ for the rind and clast interior are $9.9 \times 10^6 \text{ cm}^{-3}$ and $9.2 \times 10^5 \text{ cm}^{-3}$ respectively (Table 1).

We assume that the interior of $\rho 02\text{-P}2$ had the same vesicle characteristics as the rind upon exit from the vent

but was subsequently modified during transport in the fountain (e.g., Mangan and Cashman 1996). The interior has approximately a 3-fold increase in vesicle volume relative to the rind, which has to be some product of continued volatile exsolution and decompressive expansion. Furthermore, a 10-fold $N_{V_{\text{tot}}}^m$ decrease between rind ($9.9 \times 10^6 \text{ cm}^{-3}$) and interior ($9.2 \times 10^5 \text{ cm}^{-3}$) indicates significant bubble coalescence.

Figure 11 includes vesicle volume comparisons at individual size ranges with both the VND per cubic mm of melt (Fig. 11a, c) and the total VVD (Fig. 11b, d). The smallest vesicles are 3 \times larger in the interior relative to the rind which is likely to be the consequence of growth in the absence of continued nucleation. A decrease in $N_{V_{\text{tot}}}^m$ from rind to interior of approximately 90% is observed for all vesicle sizes (Fig. 11a, c). This can only be a consequence of coalescence and accounts for the shift of the distribution by about 3 orders of magnitude toward larger sizes. Pumice clast $\rho 20\text{-P}5$ and transitional clast $\rho 11\text{-T}19$ (Fig. 6f) also contain contrasting rind and interior textures and exhibit a similar decrease in VND (Fig. 10), thinning of glass walls, and increase in vesicle size from the rind to the interior (Fig. 8). Like $\rho 02\text{-P}2$, their interiors must have continued to expand, via a combination of bubble growth and coalescence (Fig. 10). Observation of film footage from the 1959 eruption indicates that the time for a parcel of magma to travel from the vent, through the fountain, to deposition is

Fig. 11 Vesicle number density and volume fraction of individual vesicle-size classes for clast $\rho 02\text{-P}2$ rind and interior. The horizontal axis represents vesicle volume in mm^3 . Bins form a geometric progression in $6/10 \log_{10}$ volume increments. Thus successive bins increase in volume by approximately a factor of 4. **a** Vesicle number density per mm^3 of matrix as a function of vesicle volume for the rind of sample $\rho 02\text{-P}2$. **b** Vesicle volume fraction as a function of vesicle volume for the rind of sample $\rho 02\text{-P}2$. **c** Vesicle number density per mm^3 of matrix as a function of vesicle volume for the interior of sample $\rho 02\text{-P}2$. **d** Vesicle volume fraction as a function of vesicle volume for the interior of sample $\rho 02\text{-P}2$



~8 s for a ~250 m fountain. Therefore, given the shallow depth of the free surface, at or very near the level of the vent, clast expansion occurred over a time interval of probably no more than 8 s.

Vesicularity contrasts between pumice and fluidal clasts

The pumiceous clasts have very high vesicularities and a coarse primary vesicle size mode at 3 to 10 mm diameter (Fig. 7). These larger diameter vesicles are subordinate or absent in all other clasts. Walls between pumice vesicles are very thin, typically 1–2 μm (Fig. 5a–c, j, l, n). In order to achieve these vesicle sizes and wall thicknesses, the pumice clasts must have gone through expansion histories similar to the core of $\rho 02\text{-P}2$ and $\rho 20\text{-P}5$. We infer that all pumiceous clasts in the 1959 ejecta have undergone significant post-fragmentation expansion in the core of the fountain (e.g., Mangan and Cashman 1996), but the quenched rims are only preserved on a small subset of the pumices.

Fluidal clasts show a wide vesicularity range with greater volumes of small vesicles and reduced abundances of vesicles >1.0 mm with respect to pumice (Fig. 7). A size mode at 150–350 μm dominates in all fluidal clasts, which is smaller than the size modes in pumice (300–500 μm and 3–10 mm). Fluidal clasts are less vesicular and (barring $\rho 17\text{-F}6$) have slightly higher $N_{\text{Vtot}}^{\text{m}}$ (Table 1) than pumices. Fluidal clasts with the highest $N_{\text{Vtot}}^{\text{m}}$ ($\rho 20\text{-F}9$, $\rho 11\text{-F}12$, and $\rho 02\text{-F}7$, Table 1) contain numerous 5–10 μm vesicles absent in pumices.

Vesicle size data are comparable for rinds (e.g., $\rho 02\text{-P}2$ and $\rho 20\text{-P}5$, Fig. 8) and the lowest-vesicularity fluidal clasts (e.g., $\rho 11\text{-F}12$ and $\rho 02\text{-F}7$, Fig. 7). Vesicle shape and spacing for fluidal and rind textures (Fig. 5i, m) reveal further similarities. These comparisons suggest that fluidal clasts represent earlier vesiculation stages of melt than do the pumices (Fig. 10).

The nature of transitional clasts

Most clasts have transitional textures with either homogeneous (Fig. 6a) or heterogeneous (Fig. 6f) vesicle populations. Only homogeneous clasts yield meaningful whole-clast VNDs and size distributions. We ignore the heterogeneous clasts in terms of whole-clast volumetric quantitative data but still use the qualitative observations and area measurements to deduce mechanisms for their formation.

Transitional clasts with homogeneous vesicle populations (Figs. 6a and 9) capture a process of transformation between textures typical of fluidal clasts (e.g., Fig. 5g) and those of pumice (e.g., Fig. 5a, j). Low-vesicularity transitional clasts (Fig. 7) $\rho 09\text{-T}29$ and $\rho 09\text{-T}82$ (Fig. 9d) have high $N_{\text{Vtot}}^{\text{m}}$ (Table 1, Fig. 7) and evenly distributed

populations of rounded and coalesced vesicles (e.g., Fig. 9e, f). VVDs for these clasts closely resemble those for fluidal clasts (Fig. 7) with volumetric peaks at 0.25-mm diameter and relatively sparse coarse vesicle populations. Vesicles in these clasts (e.g., $\rho 09\text{-T}29$, Fig. 9d–f) are slightly larger, more irregular and more closely spaced than in the lowest vesicularity fluidal clasts (e.g., $\rho 02\text{-F}7$, Fig. 5g–i) but are similar to higher-vesicularity fluidal clasts (e.g., $\rho 17\text{-F}6$, Fig. 5d–f). Based on VVDs and textural similarities between low-vesicularity transitional and fluidal clasts, the increase in vesicularity corresponds to a maturation of vesicle textures.

High-vesicularity transitional clasts (Fig. 7) $\rho 11\text{-T}13$ (Fig. 6a), $\rho 02\text{-T}40$, and $\rho 02\text{-T}37$ have a ~1 mm thick quenched glassy rim surrounding an evenly distributed population of mostly round, multiple-sized vesicles. This set of clasts has relatively similarly shaped VVDs (Fig. 7) lacking significant vesicles >1 mm and vesicularities (68% to 81%, Table 1) that lie between fluidal (64% to 68%, Table 1) and pumice (86% to 90%, Table 1). As stated above, the highest-vesicularity transitional clast, $\rho 09\text{-T}6$ (Fig. 9a) has a texture and VVD (Fig. 7) intermediate between other high-vesicularity transitional (e.g., $\rho 11\text{-T}13$, Fig. 6a) and pumice (e.g., $\rho 09\text{-P}1$, Fig. 5a) clasts. Using the texture of clast $\rho 09\text{-T}6$ as a bridge between transitional and pumice morphologies, we suggest a proportion of the smaller vesicles expanded to form larger vesicles, resulting in VVDs skewed toward coarser populations. In Fig. 10, the trend from transitional clasts to pumice is seen as an increase in vesicularity accompanied by decrease in $N_{\text{Vtot}}^{\text{m}}$ (Table 1). The latter implies that expansion must have been accommodated by some degree of vesicle coalescence. The interior of the thinly rimmed clast, $\rho 09\text{-T}6$ (Fig. 9a) is, in every sense, a less mature (i.e., lower-vesicularity) form of that seen in the expanded pumice. Based on the comparison of pumiceous and fluidal textures above, we believe that homogeneous transitional clasts preserve varying stages of quenched textures intermediate between those two end members.

Heterogeneous transitional clasts (Fig. 6f) capture in situ, but patchy, vesiculation processes on the path from fluidal to pumiceous texture. These clasts contain regions characterized by larger vesicles with coalescence shapes; these regions are typically concentrated toward the clast center (Fig. 6f, j–l). The more glassy regions contain smaller vesicles and are often located along quenched rims or near the edges of clasts (Fig. 6f–i), but these glassy rim regions are much wider and more irregular than the rinds in homogeneous transitional (Figs. 6a and 9) or pumiceous (Fig. 5j) clasts. In order to form larger regions of small, widely-spaced vesicles, portions of the transitional clasts with wide rims (Fig. 6f) must have quenched radially inward more rapidly than the thinly-rimmed homogeneous transitional (Fig. 6a) and pumice clasts.

Textural variability among clasts within samples

Given the estimated duration of accumulation at the study site, each sample represents sedimentation of approximately 2.5 to 3 h. The diversity of pyroclasts in each sample therefore reflects the heterogeneity of the melt phase in the shallow conduit as well as textural maturation in the fountain on these short time scales.

In every sample, similar variations exist in the VVD and textural range of erupted material. Figure 9 depicts the textural variability in clasts from one sample ($\rho 09$). These are the lowest and highest vesicularity transitional clasts in the study and are most similar to fluidal and pumiceous textures respectively. If melt approximating $\rho 09$ -T82 (Fig. 9d) continued to vesiculate, it is conceivable that the small (5–30 μm) vesicles (e.g., Fig. 9f) would expand, larger vesicles with thin film boundaries would coalesce, early-coalesced vesicles would relax, and then additional coalescence would yield a texture comparable to $\rho 09$ -T6 (e.g., Fig. 9a). A decrease in $N^{\text{m}}_{\text{Vtot}}$ ($1.1 \times 10^7 \text{ cm}^{-3}$ to $4.1 \times 10^6 \text{ cm}^{-3}$, Table 1), and the VVD comparison for these two clasts (Fig. 7), confirm this as a possible trend, resulting in loss of the vesicle population below 30 μm and an increase in proportions of vesicles $>1 \text{ mm}$. A similar trend is seen by comparing $N^{\text{m}}_{\text{Vtot}}$ and VVD for clasts $\rho 11$ -F12 and $\rho 11$ -T13 (Fig. 7). Textural evidence of varying degrees of post-fragmentation vesiculation implies different cooling histories for fluidal and pumiceous clasts. Additionally, cooling rate contrasts are evident within individual clasts containing regions of differing vesicularity, e.g., clasts with dense glassy rinds and more-vesicular interiors.

Within a single sample, the simple post-fragmentation vesiculation trend discussed above, from fluidal to transitional to pumice, does not always hold. For example, although there is a trend between end-member-vesicularity transitional clasts in sample $\rho 09$, the pumice clast from that sample ($\rho 09$ -P1, Fig. 7) contains a very slightly (~ 2) larger $N^{\text{m}}_{\text{Vtot}}$ than the high-vesicularity transitional clast, $\rho 09$ -T6. Additionally, the last sample erupted, $\rho 02$, contains two transitional clasts; one $N^{\text{m}}_{\text{Vtot}}$ is ~ 1.5 times lower ($\rho 02$ -T37, Fig. 7) than the co-erupted fluidal clast ($\rho 02$ -F7), and the other is ~ 1.5 times higher ($\rho 02$ -T40, Fig. 7). Minute differences such as these can be explained by variable nucleation rates associated with a cross-conduit gradient in ascent rate, as melt ascends more quickly along the axis than the conduit walls (Adams et al. 2006; Sable et al. 2006; Taddeucci et al. 2004). Small variations in nucleation rate may also be attributed to minute differences in surface tension due to temperature, volatile content, or inherited magma heterogeneity. This gives textural diversity to the melt prior to fragmentation which, in the case of Kilauea Iki, is then overprinted by variable amounts of post-fragmentation expansion.

Textural variability within clast types and among samples

The variability among samples, and similar types of clasts in each sample, gives information associated with changes on a longer time scale of 4 to 5 days, during episode 1 eruption and deposition.

The lowest vesicle number density is from sample $\rho 17$ (Table 1) which also contains the largest clasts (Fig. 4b). The fluidal clast, $\rho 17$ -F6 (Fig. 5d), is unlike others in its clast category, containing coalescence textures (Fig. 5e, f), and an oversized vesicle (~ 4 -cm diameter) and lacks vesicles smaller than 20- μm diameter. Additionally, this clast has a slightly lower $N^{\text{m}}_{\text{Vtot}}$ than contemporaneously erupted pumice ($\rho 17$ -P1, Table 1). These differences may record the fact that the eruption began as a dike, and the deep conduit maintained this geometry throughout episode 1. With time, more mature and degassed ($\sim 2 \times$ lower $N^{\text{m}}_{\text{Vtot}}$ than other fluidal clasts) magma may have been entrained from now-stagnant conduit regions surrounding the main eruptive pathway. The entrained magma was not in residence long enough to outgas fully, as evident by the still relatively high $N^{\text{m}}_{\text{Vtot}}$, and was probably incorporated as a result of increasing eruption intensity during a short-lived fountain-height peak ($\sim 320 \text{ m}$) coinciding with deposition of the maximum-sized clasts (Fig. 3b).

The last sample erupted, $\rho 02$, has a unique combination of characteristics. It has the greatest number of pumice clasts (Fig. 4), a clear example of post-fragmentation expansion (Fig. 5j–l), a unimodal VVD ($\rho 02$ -T40, Fig. 7), the smallest volume of vesicles in bins $>1 \text{ mm}$ (Fig. 7), and the smallest vesicle diameter peak (0.15 mm) across all clasts (e.g., $\rho 02$ -T37 & $\rho 02$ -T40, Fig. 7). The combination of these factors rules out an explanation involving both a high degree of coalescence and multiple nucleation events. Furthermore, clasts in this sample were erupted through the lava lake surface.

Discussion*Rinds and clast interiors*

The relationship between rind and interior of individual clasts is pivotal to understanding the diversity of micro-textures in all the episode 1 products. Rinds, which we infer to be quenched rapidly after fragmentation, contain high proportions of small vesicles, which limited opportunity for bubble growth or coalescence, so that the rind vesicle textures closely approximate magma texture during fragmentation. Given the small size of the clasts, it follows that textures preserved in the interior of rimmed clasts (1) developed after quenching of the rind and (2) evolved from more primitive vesicle textures closely resembling those of

the associated rinds. We can use the quantitative contrasts between rinds and interiors to constrain which processes took place between fragmentation and final quenching of clast interiors. Vesiculation processes potentially contributing to the contrast include: continued nucleation, bubble growth by expansion and/or diffusion, bubble coalescence, and bubble escape or collapse (Fig. 10).

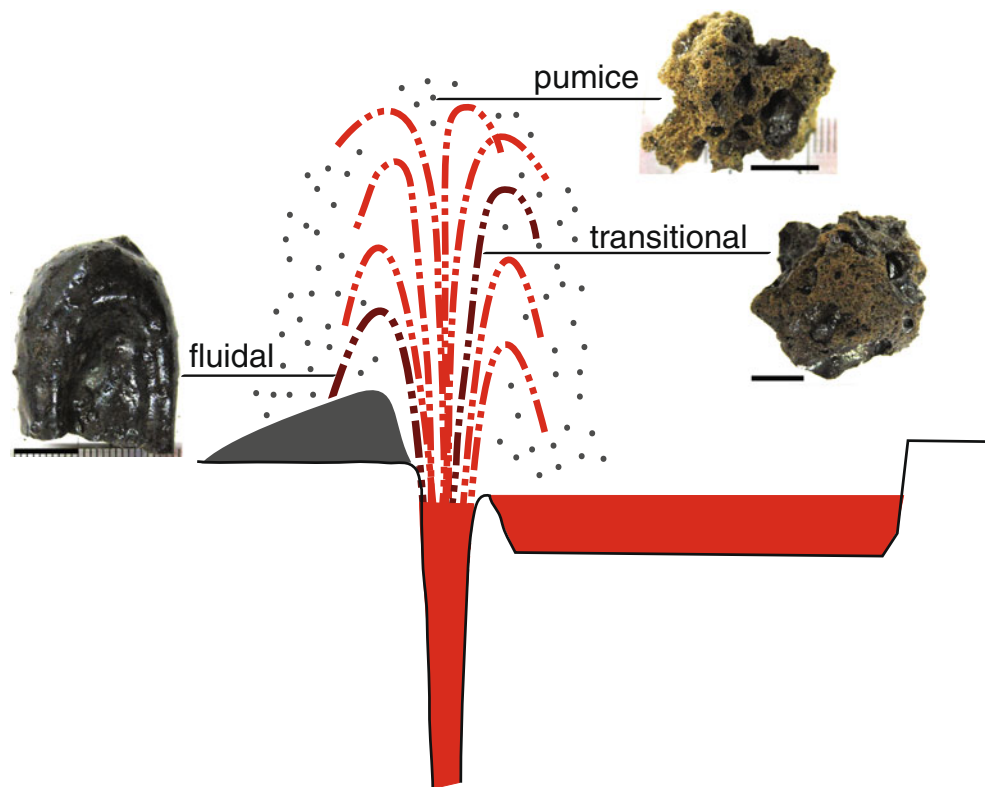
For each pair of rind and interior textures, the trend is for a decrease in VND and increase in V_G/V_L (Fig. 10). Based on the interpretation for clast $\rho 02\text{-P}2$ above, the bubble population in the interiors evolved via a combination of coalescence and continued bubble growth after clast rinds quenched to lock in more-primitive vesicle populations.

The data from Table 1 and the graph in Fig. 10 can be used in simple calculations to approximate the components of clast expansion (growth and coalescence). By separating the amount of vesicle volume increase (vertical change) and vesicle number density decrease (horizontal change) represented on Fig. 10, the relative amounts of growth versus coalescence can be determined. Using vesicle volume and the vesicle number density for the two zones of clast $\rho 02\text{-P}2$, the mean diameter for a single bubble is $47\ \mu\text{m}$ within the rind (volume = $5.6 \times 10^{-5}\ \text{mm}^3$) and $118\ \mu\text{m}$ within the interior (volume = $8.6 \times 10^{-4}\ \text{mm}^3$), a factor of 2.5 difference. For the rind of clast $\rho 02\text{-P}2$ to achieve the same vesicle to melt ratio as the interior (1 on Fig. 10), the average volume of bubbles in the rind must increase from $5.6 \times 10^{-5}\ \text{mm}^3$ to $8.1 \times 10^{-5}\ \text{mm}^3$ ($53\ \mu\text{m}$ mean diameter), a

change which would account for a factor of 1.1 (47 to $53\ \mu\text{m}$) of the total factor of 2.5 increase in mean vesicle diameter. The amount of coalescence necessary to achieve the observed decrease in VND from rind to interior requires the mean bubble volume at location 1 to increase from $8.1 \times 10^{-5}\ \text{mm}^3$ to $8.6 \times 10^{-4}\ \text{mm}^3$ (a volume increase of $7.8 \times 10^{-4}\ \text{mm}^3$). Therefore, coalescence accounts for a factor of 2.2 of the mean vesicle diameter increase (53 to $118\ \mu\text{m}$) from rind to interior, and the mean vesicle volume increases by a factor of 9.7. Based on these calculations, after rind-approximating bubbles expand via growth by a factor of 1.1, up to 10 bubbles of mean diameter must coalesce to achieve the mean volume of bubbles in clast interiors. Growth and coalescence occurs within 8 s of travel time in the fountain, therefore $8 \times 10^{-4}\ \text{mm}\ \text{s}^{-1}$ is the maximum growth rate and 1 events s^{-1} is the minimum coalescence rate which increases the diameter at a rate of $8 \times 10^{-3}\ \text{mm}\ \text{s}^{-1}$.

For comparison purposes, the same calculations can be made to account for the degree of growth and coalescence for a clast such as $\rho 09\text{-P}1$ originating with the vesicle volume and VND as seen in the rind of $\rho 02\text{-P}2$. The mean vesicle diameter increases by a factor of 1.44 from $47\ \mu\text{m}$ to $68\ \mu\text{m}$, significantly less than the increase from rind to interior for clast $\rho 02\text{-P}2$. Growth only, from $\rho 02\text{-P}2\text{R}$ to location 2 on Fig. 10, would account for a factor of 1.17 mean diameter increase (from 47 to $55\ \mu\text{m}$) resulting in a bubble with a mean volume of $8.9 \times 10^{-5}\ \text{mm}^3$. Coalescence only, from location 2 on Fig. 10 to $\rho 09\text{-P}1$, would account for a factor

Fig. 12 Clast type photographs and location of origin within the Kīlauea Iki fountain. Cartoon of Kīlauea Iki fountain and conduit with adjacent cone and lava lake. Clast types and relative locations of quenching within the fountain are indicated by line adjacent to clast. Scale bar below each clast equals 1 cm length. Cartoon is not to scale



of 1.24 mean diameter increase (from 55 to 68 μm) resulting in a final bubble volume of $1.6 \times 10^{-4} \text{ mm}^3$ which is a factor of 1.8 increase in mean vesicle volume. Therefore, growth occurs at a maximum rate of $9.9 \times 10^{-4} \text{ mm s}^{-1}$ and coalescence occurs at a minimum rate of 0.22 events s^{-1} , increasing diameter at a rate of $1.5 \times 10^{-3} \text{ mm s}^{-1}$. By comparing these two end members ($\rho 02\text{-P}2$ and $\rho 09\text{-P}1$), it is clear that coalescence plays a more significant role than growth in post-fragmentation expansion.

Origin of fluidal and pumice textures in homogeneous clasts

The strong microtextural similarities between (1) the rinds of rimmed clasts and fluidal clasts lacking rinds and (2) the interior of rimmed clasts and rind-free pumice are the keys to interpreting the homogeneous clasts. We infer that diversity in clast texture is a product of location, trajectory, and residence time within the fountain. Figure 12 indicates the inferred location of origin within the fountain for each of the clast types. This is supported by the eyewitness observations of dark quenched clasts falling from the margin of the fountain and the fact that pumice clasts were observed to rise to the full height of the fountain or even beyond, entering the dilute convective plume (Richter et al. 1970).

Fluidal clasts have high proportions of small vesicles that quenched rapidly after fragmentation and underwent limited bubble growth and coalescence with respect to pumice. In order to maintain large populations of small vesicles (e.g., $\rho 20\text{-F}9$, $\rho 11\text{-F}12$, $\rho 02\text{-F}7$), the fluidal clasts, like clast rinds, must have quenched shortly after fragmentation, without experiencing significant post-fragmentation expansion (Fig. 12).

Pumice clasts contain the greatest volume of large vesicles, with strong bimodal VVDs (Fig. 7) that closely resemble the interiors of clasts with rinds (Fig. 8a, b). We infer that they went through a similar extended history of post-fragmentation expansion; either never forming rinds or losing the rinds as a result of breakup in the jet or upon landing.

The significance and origin of transitional clasts

Transitional clasts can generally be considered to preserve textures that quenched at some point along the path of melt evolution between fluidal and pumice types. Homogeneous transitional clasts (Figs. 6a–e and 9) traveled a path through the fountain that limited expansion to less than that experienced by pumice. Heterogeneous transitional clasts (Fig. 6f–l) formed in a similar way to those pumice clasts with existing rind and interior pairs (e.g., $\rho 02\text{-P}2$, Fig. 5j–n), where the exterior of the clast quenched while the

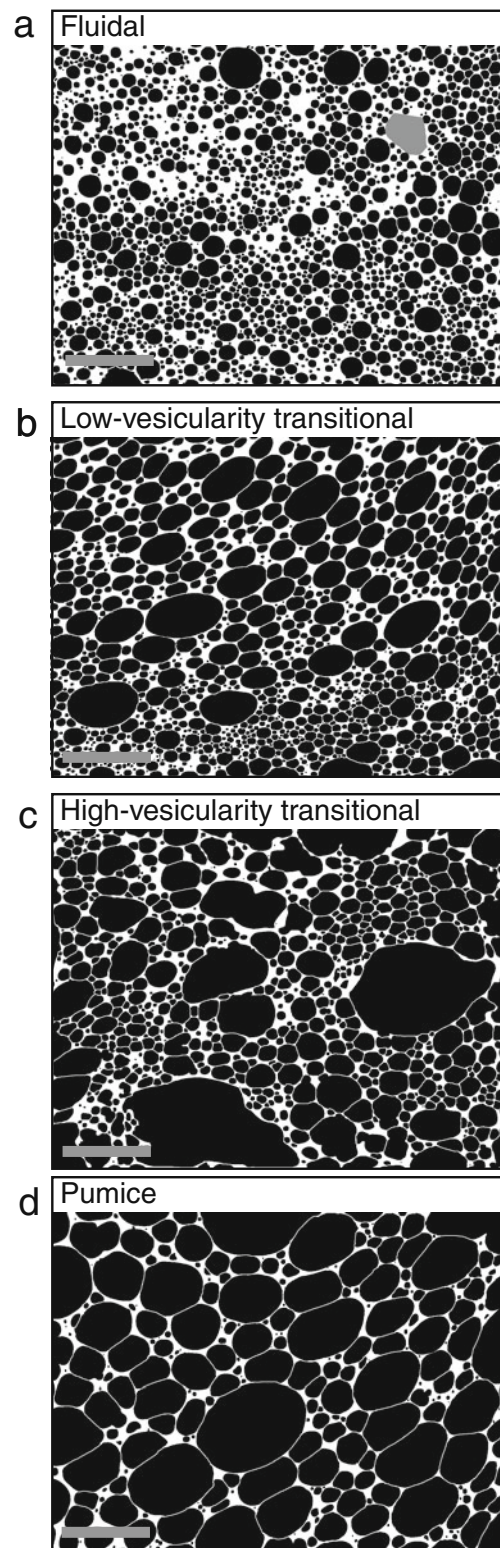


Fig. 13 Collection of $25\times$ magnification grayscale SEM images representing fluidal to pumice transition within the fountain. Fluidal (a), homogeneous-transitional (b, c), and pumice (d) clasts in order of increasing vesicularity. Full vesicle evolution for Hawaiian fountains at Kilauea Iki originates with textures approximating a and mature to textures approximating d. Scale=1.0 mm

interior continued to expand, though to a lesser degree than rimmed clasts with pumiceous interiors.

Post-fragmentation evolution of clasts

Thermal gradients within the fountain drive textural diversity within Hawaiian tephra (Fig. 12). Clasts within the fountain center remain hot longer and undergo minimal cooling before sedimentation, yielding clasts with mature vesicle populations. Clasts transported in the fountain margins quench more rapidly and result in less-vesicular fluidal textures (Fig. 12) preserving conduit approximating textures without a significant overprint of post-fragmentation expansion. Hot gases streaming through the fountain glaze the outside of clasts (Thordarson et al. 1996) and superimpose a glassy sheen on the exterior of clasts.

Figure 13 represents the progression of post-fragmentation expansion originating with fluidal-type melt and ending in pumice morphology. Initially fragmented melt (e.g., Fig. 13a) contains abundant small, round bubbles (5–10- μm diameter) with thick glass walls and evenly distributed larger bubbles. The proportion of small bubbles decreases due to growth and coalescence, resulting in larger numbers of bubbles between ~15–90- μm diameters (e.g., Fig. 13b). Bubbles continue to coalesce and grow, via further fountain-insulated expansion, until bubbles >1 mm in diameter dominate at the expense of smaller sizes (e.g., Fig. 13c), resulting in highly vesicular pumice (Fig. 13d).

Distribution and sedimentation of clasts from the fountain would have been strongly affected by the northeasterly trade winds, relative clast density, and location within the fountain. Fluidal clasts from the fountain margins are typically the densest and were likely deposited in a weakly ellipsoidal geometry close to the vent. Because the very low density pumice clasts originate from the upper portion of the fountain, the distribution range was more wind-attenuated resulting in greater sedimentation downwind of the vent (e.g. Swanson et al. 1979). Transitional clasts have the widest density range and were therefore less preferentially distributed, instead occurring throughout the entire deposit.

Conclusion

Our findings reveal more clearly the processes occurring in the fountain for a classic Hawaiian explosive eruption. A population of mechanically coupled bubbles, which is represented by the smallest vesicle population we have studied, gives validity to the 1-phase rise-speed dependent (RSD) model for Hawaiian eruptions (Wilson 1980; Wilson and Head 1981; Head and Wilson 1987; Parfitt and Wilson 1995; Parfitt and Wilson 1999; Slezin 2003). Under equilibrium degassing conditions

for Kilauea Iki's reservoir-equilibrated magma, Gerlach (1986) suggests a depth of <150 m for H_2O exsolution. This shallow level of degassing means that magma must be transported to these depths by driving forces other than those relating to upward momentum imparted by the near-surface exsolution of H_2O (Gerlach 1986). This could have been achieved through upward forcing by a previously exsolved gas phase (e.g., CO_2) or due to rise of magma as a result of excess reservoir pressure imparted by the influx of new magma from 40 to 60 km depth (Eaton et al. 1987). This raises the question as to what specific dynamics result in characteristic Hawaiian fountaining and over what depth range and time scales these dynamics pertain.

The vesicle size distributions imparted to the 1959 magma by processes occurring during conduit flow prior to fragmentation are overprinted by extended vesiculation within the fountain. Variable cooling rates, inferred to be related to radial thermal gradients in the fountain and clast sizes, resulted in the formation of pyroclast textures with varying histories of vesicle growth. Clasts within the center of the fountain remained thermally insulated, and bubbles continued to expand and coalesce during transportation, resulting in the formation of pumice and the high-vesicularity transitional clasts. Clasts traveling at the outer edges of the fountain quenched most quickly, locking in higher abundances of small vesicles and producing fluidal clast morphologies.

Acknowledgements We thank Julia Hammer, Gary Barnes, Jacopo Taddeucci, and an anonymous reviewer for their helpful feedback on this work prior to publication. The breadth of this data set was greatly helped by Maria Janebo's diligent and thorough assistance with laboratory work. We are also very grateful to Thomas Shea for his invaluable MATLAB program, FOAMS. Thanks also to Lisa Swinnard and Penny Larin for their help with rocks and stratigraphical logs. This research was funded by NSF grants EAR-0709303 and OISE-0811838 and published under employment with IM Systems Group on contract at NOAA Pacific Services Center.

References

- Adams NK, Houghton BF, Hildreth W (2006) Abrupt transitions during sustained explosive eruptions: examples from the 1912 eruption of Novarupta, Alaska. *Bull Volcanol* 69:189–206
- Bertagnini A, Calvari S, Coltelli M, Landi P, Pompilio M, Scribano V (1990) The 1989 eruptive sequence. In: Barberi F, Bertagnini A, Landi P (eds) Mt. Etna: the 1989 eruption. Giardini, Pisa, pp 10–22
- Bottinga Y, Weill DF (1970) Densities of liquid silicate systems calculated from partial molar volumes of oxide components. *Am J Sci* 269:169–182
- Cashman KV, Mangan MT (1994) Physical aspects of magmatic degassing II: constraints on vesiculation processes from textural studies of eruptive products. In: Carroll MR, Holloway JR (eds) Volatiles in magmas. Reviews in mineralogy. Mineralogical Society of America, Fredricksberg, pp 447–478
- Eaton JP, Richter DH, Krivoy HL (1987) Cycling of magma between the summit reservoir and Kilauea Iki lava lake during the 1959

- eruption of Kīlauea volcano. In: Decker RW, Wright TL, Stauffer PH (eds) *Volcanism in Hawai'i*. US Geol Surv Prof Pap, 1350: 1307–1334
- Fedotov SA, Chirkov AM, Gusev NA, Kovalev GN, Slezin YB (1980) The large fissure eruption in the region of Plosky Tolbachik volcano in Kamchatka, 1975–1976. *Bull Volcanol* 43:47–60
- Gardner JE, Thomas RME, Jaupart C, Tait S (1996) Fragmentation of magma during Plinian volcanic eruptions. *Bull Volcanol* 58:144–162
- Gerlach TM (1986) Exsolution of H₂O, CO₂, and S during eruptive episodes at Kīlauea volcano, Hawai'i. *J Geophys Res* 91:12177–12185
- Gurioli L, Harris AJL, Houghton BF, Polacci M, Ripepe M (2008) Textural and geophysical characterization of explosive basaltic activity at Villarrica volcano. *J Geophys Res* 113:B08206. doi:10.1029/2007JB005328
- Head JW, Wilson CJN (1987) Lava fountain heights at Pu'u Ō'ō Kīlauea, Hawai'i: indicators of amount and variations of exsolved magma volatiles. *J Geophys Res* 92:13715–113719
- Heliker C, Mattox TN (2003) The first two decades of the Pu'u Ō'ō-Kupaianaha eruption: chronology and selected bibliography, the Pu'u Ō'ō-Kupaianaha eruption of Kīlauea volcano, Hawai'i: the first 20 years. US Geol Surv Prof Pap 1676:1–27
- Houghton BF, Wilson CJN (1989) A vesicularity index for pyroclastic deposits. *Bull Volcanol* 51:451–462
- Klug C, Cashman KV, Bacon CR (2002) Structure and physical characteristics of pumice from the climactic eruption of Mount Mazama (Crater Lake), Oregon. *Bull Volcanol* 64:486–501
- Lautze NC, Houghton BF (2007) Linking variable explosion style and magma textures during 2002 at Stromboli volcano, Italy. *Bull Volcanol* 69:445–460
- Mangan MT, Cashman KV (1996) The structure of basaltic scoria and reticulite and inferences for vesiculation, foam formation, and fragmentation in lava fountains. *J Volcanol Geotherm Res* 73:1–18
- Mangan MT, Cashman KV, Newman S (1993) Vesiculation of basaltic magma during eruption. *J Geol* 21:157–160
- Mastin LG, Christiansen RL, Thornber CR, Lowenstern JB, Beeson M (2004) What makes hydromagmatic eruptions violent? Some insights from the Keanakakoi Ash, Kīlauea volcano, Hawai'i. *J Volcanol Geotherm Res* 137:15–31
- Murata KJ, Richter DH (1966) Chemistry of the lavas of the 1959–60 eruption of Kīlauea Volcano, Hawai'i. In: *The 1959–60 eruption of Kīlauea volcano, Hawai'i*. US Geol Surv Prof Pap, 537-A:A1–A26
- Parfitt EA, Wilson L (1995) Explosive volcanic eruptions IX. The transition between Hawaiian-style lava fountaining and Strombolian explosive activity. *Geophys J Int* 121:226–232
- Parfitt EA, Wilson L (1999) A Plinian treatment of fallout from Hawaiian lava fountains. *J Volcanol Geotherm Res* 88:67–75
- Richter DH, Eaton JP, Murata KJ, Ault WU, Krivoy HL (1970) Chronological narrative of the 1959–60 eruption of Kīlauea volcano, Hawai'i. In: *The 1959–60 eruption of Kīlauea volcano, Hawai'i*. US Geol Surv Prof Pap, 537-E:E1–E73
- Sable JE, Houghton BF, Del Carlo P, Coltelli M (2006) Changing conditions of magma ascent and fragmentation during the Etna 122 BC basaltic Plinian eruption: evidence from clast micro-textures. *J Volcanol Geotherm Res* 158:333–354
- Shea T, Houghton BF, Gurioli L, Cashman KV, Hammer JE, Hobden BJ (2009) Textural studies of vesicles in volcanic rocks: an integrated methodology. *J Volcanol Geotherm Res* 190:271–289
- Slezin YB (2003) The mechanism of volcanic eruptions. *J Volcanol Geotherm Res* 122:7–50
- Swanson DA, Duffield WA, Jackson DB, Peterson DW (1979) Chronological narrative of the 1969–71 Mauna Ulu eruption of Kīlauea volcano, Hawai'i. US Geol Surv Prof Pap 1056:1–55
- Taddeucci J, Pompilio M, Scarlato P (2004) Conduit processes during the July–August 2001 explosive activity of Mt. Etna (Italy): inferences from glass chemistry and crystal size distribution of ash particles. *J Volcanol Geotherm Res* 137:33–54
- Thordarson T, Self S, Óskarsson N, Hulsebosch T (1996) Sulfur, chlorine and fluorine degassing and atmospheric loading by the 1783–1784 AD Laki (Skaftár Fires) eruption in Iceland. *Bull Volcanol* 58:205–225
- Walker GPL, Croasdale R (1972) Characteristics of some basaltic pyroclastics. *Bull Volcanol* 35:303–317
- Wilson L (1980) Relationships between pressure, volatile content and ejecta velocity in three types of volcanic explosions. *J Volcanol Geotherm Res* 8:297–313
- Wilson L, Head JW (1981) Ascent and eruption of basaltic magma on the Earth and Moon. *J Geophys Res* 86:2971–3001